Nanoscale

PAPER

View Article Online
View Journal

Cite this: DOI: 10.1039/d5nr04623h

Spinel $ZnMn_2O_4$/Ni-based metal–organic framework hybrid composite for high-performance asymmetric supercapacitors

Abinash Kumararaj,[a] Kamala Bharathi Karuppanan[b] and Geetha Arunachalam *[a]

Creation of advanced electrode materials with superior electrochemical performance is essential for advancing next-generation supercapacitors. Integrating spinel oxide with metal–organic frameworks significantly enhances the supercapacitor's electrochemical performance, energy, and power density. In this study, we synthesised a $ZnMn_2O_4$/Ni-MOF composite *via* the solvothermal technique and examined its structural and morphological characteristics using X-ray diffraction (XRD), Fourier transform infrared (FT-IR), spectroscopy, high-resolution scanning electron microscopy (HR-SEM), and X-ray photoelectron spectroscopy (XPS). Further, the electrochemical analysis at a three-electrode system demonstrates exceptional performance characteristics, showing a specific capacitance (C_s) of 623 F g^{-1} at 1 A g^{-1} and impressive cyclic endurance, with 82% capacity retention and coulombic efficiency of 98% after 5000 cycles. *Ex situ* XRD and SEM analysis are employed to study the structural and morphological changes after cycling the electrodes. The aqueous asymmetric supercapacitor (AASC) configuration shows a C_s of 155 F g^{-1} at 1 A g^{-1}, with a remarkable energy density of 55 Wh kg^{-1} and power density of 800 W kg^{-1}. An asymmetric supercapacitor (ASC) device is also developed, and it exhibits a C_s of 15 F g^{-1} at 1 A g^{-1}. Additionally, its efficacy is evaluated by connecting two ASCs in series to power the LEDs. These results demonstrate the excellent performance of the $ZnMn_2O_4$/Ni-MOF composite, which can be used in real-life applications to provide advanced energy storage solutions.

Received 1st November 2025,
Accepted 18th March 2026

DOI: 10.1039/d5nr04623h

rsc.li/nanoscale

Introduction

Due to the rapid growth of renewable energy sources and the significant challenges posed by global warming and the worldwide energy crisis, the need for highly effective energy storage technology has substantially increased.[1] These challenges demand investigations into innovative energy storage systems; one such system is electrochemical capacitors, also known as supercapacitors (SCs) or ultracapacitors, which have attracted considerable attention due to their unique features.[2] SCs, an innovative energy storage and conversion technology that integrates traditional physical capacitors and batteries, exhibit significant potential and advantages, including rapid charge–discharge capabilities, high charge–discharge efficiency, extended cyclic life, and elevated power density.[3] Significant breakthroughs in electrochemical efficiency have made supercapacitors one of the most attractive choices for next-generation power devices.[4] SCs, especially asymmetric supercapacitors (ASCs), have emerged as promising candidates due to their exceptional performance. ASCs have garnered interest due to their ability to integrate the advantages of both batteries and supercapacitors. Their ability to provide extended cyclic life, enhanced energy density, and superior power density compared to traditional capacitors renders them suitable for a wide range of applications. In ASCs, two different electrode materials are used, which can enhance the operational voltage range and specific capacitance of the device, which potentially transforms it into a portable power supply.[5,6]

Metal–organic frameworks (MOFs) feature three-dimensional network-like crystalline structures comprising an inorganic metal centre that serves as a source of metal active sites with pseudocapacitive behaviour and an organic ligand that forms a carbon matrix. This results in a controllable microporous structure with high specific surface area and large pore volume, thus demonstrating significant potential for supercapacitor applications.[7] Transition metals are well known for their coordination with organic linkers and other metal centers, providing benefits such as multiple valence

[a]Department of Physics and Nanotechnology, Faculty of Engineering and Technology, SRM Institute of Science and Technology, Kattankulathur, Chengalpattu 603 203, Tamil Nadu, India. E-mail: geethaa@srmist.edu.in
[b]Thin Film Energy Storage Laboratory, Department of Physics and Nanotechnology, SRM Institute of Science and Technology, Kattankulathur, Chengalpattu 603 203, Tamil Nadu, India

states, diverse electrochemical characteristics, and redox behaviour.[8] Nickel-based metal–organic framework (Ni-MOF) is frequently used in supercapacitor electrodes due to its high specific activity, high porosity, abundant active sites, and high stability in alkaline environments. However, it experiences structural degradation (collapse of the pore structure) over time and during continuous charge–discharge cycles.[9]

Metal oxides are significant functional materials recognised for their varied electrical, magnetic, and catalytic properties, rendering them valuable in numerous applications.[10] Among metal oxides, spinel oxides (AB_2O_4) or spinel structure-based nanomaterials demonstrate high theoretical capacitance and consistent electrochemical performance. The electrochemical performance of several ternary spinel compounds was increased by combining manganite (AMn_2O_4) with another metal oxide (Zn), and these nanomaterials were used as energy storage electrodes in supercapacitors.[11] Zinc manganese oxide ($ZnMn_2O_4$) demonstrates significant potential as a supercapacitor electrode material owing to its high theoretical capacity and non-toxic, ecologically benign composition. The spinel structure is composed of bivalent Zn^{2+} ions present in tetrahedral sites and trivalent Mn^{3+} ions in octahedral sites.[12] In addition, the spinel $ZnMn_2O_4$ offers substantial structural stability during charge–discharge cycling, which extends cycle life.[13]

The $ZnMn_2O_4$/Ni-MOF composite outperforms earlier reported spinel/MOF hybrids due to its synergistic effect, multi-redox system and improved heterostructure design. $ZnMn_2O_4$ promotes Mn-based redox activity, whereas Ni-MOF adds Ni^{2+}/Ni^{3+} electroactive sites and a porous framework to improve electrolyte accessibility and ion diffusion. The intimate interfacial interaction between the spinel oxide and the MOF matrix enhances charge-transfer kinetics while mitigating structural degradation during cycling. The $ZnMn_2O_4$/Ni-MOF system outperforms other spinel/MOF composites in terms of capacitance, rate capability, and cycle stability due to its unique combination of multi-metal redox activity, mesoporous design, and enhanced structural stability.[14–16] In this study, we report the synthesis of the $ZnMn_2O_4$/Ni-MOF composite using a solvothermal method and subsequently evaluate its structural, morphological, and electrochemical properties for supercapacitor applications. The electrochemical performance of the $ZnMn_2O_4$/Ni-MOF composite is assessed in both three- and two-electrode setups. In a three-electrode configuration, $ZnMn_2O_4$/Ni-MOF demonstrated exceptional performance characterised by discrete redox peaks, a high $C_{s,}$ and remarkable cyclic reliability. In the two-electrode asymmetric configuration, $ZnMn_2O_4$/Ni-MOF exhibited exceptional energy and power densities, underscoring its high-performance in supercapacitor applications and further strengthening the ASC's potential for integration into portable electronic systems. These findings position $ZnMn_2O_4$/Ni-MOF as an attractive electrode material, markedly enhancing the utility of MOF-based materials in energy storage systems. The structural, morphological, and electrochemical results obtained are presented and discussed in this manuscript.

Experimental section

Materials

Zinc(II) acetate dihydrate, manganese(II) acetate tetrahydrate, urea, nickel(II) chloride hexahydrate ($NiCl_2{\cdot}6H_2O$), terephthalic acid ($C_6H_4(CO_2H)_2$), potassium hydroxide (KOH), polyvinyl alcohol (PVA), polyvinylidene fluoride (PVDF), carbon black, *N*-methyl-2-pyrrolidone (NMP) and ethanol was purchased from Sigma Aldrich Chemical Reagent Co. Ltd and Sisco Research Laboratories Pvt. Ltd.

Synthesis of $ZnMn_2O_4$ microspheres

In a standard synthesis, 0.1 M of $Zn(CH_3COO)_2{\cdot}2H_2O$, 0.2 M of $Mn(CH_3COO)_2{\cdot}4H_2O$, and 1.7 M of urea were dissolved in 50 mL of anhydrous ethanol by stirring for 30 minutes. The solution was subsequently placed in a 100 mL Teflon-lined stainless-steel autoclave and heated at 180 °C for 12 hours. The solid product was centrifuged, washed three times with deionised water and anhydrous ethanol, then dried at 60 °C overnight, and subsequently calcined at 500 °C for 5 hours to yield $ZnMn_2O_4$ microspheres.

Synthesis of the $ZnMn_2O_4$/Ni-MOF composite

In the synthesis process of the $ZnMn_2O_4$/Ni-MOF composite, 0.5 g of pre-synthesized $ZnMn_2O_4$ is dispersed in 20 mL of ethanol and stirred continuously for 30 minutes, named as solution A. Separately, 0.25 M of terephthalic acid and 0.5 M of $NiCl_2{\cdot}6H_2O$ were dissolved in 30 mL of *N*,*N*-dimethylformamide (DMF) under stirring for 30 minutes, named as solution B. Solution A was subsequently mixed with solution B, and the resultant mixture was stirred for an additional hour to guarantee equal dispersion. The homogeneous mixture was then transferred into a 100 mL autoclave and underwent a solvothermal reaction at 120 °C for 24 hours in a hot air oven. After reaching room temperature, the final yield was obtained using centrifugation, repeatedly washed with C_2H_5OH and DI water to eliminate impurities, and subsequently dried at 80 °C overnight. The dried product was ground into a fine powder to yield the final $ZnMn_2O_4$/Ni-MOF composite, as shown in the Fig. 1. For comparison, the pure Ni-MOF is synthesised using the above process, excluding the incorporation of $ZnMn_2O_4$ into the solution B.

Characterization

The samples were carefully characterised using several analytical techniques. X-ray diffraction (XRD) was performed using a PANalytical powder diffractometer with Cu Kα radiation to ascertain the crystalline structure. Fourier transform infrared (FTIR) spectroscopy was conducted with a Shimadzu IR Tracer 100 spectrometer across the 400 to 4000 cm^{-1} range to ascertain the functional groups contained in the sample. The morphological and elemental composition were analysed using high-resolution scanning electron microscopy (HRSEM) with a Thermo Scientific Apreo S equipment. The surface chemical composition of the composite was examined using X-ray photoelectron spectroscopy (XPS) with a PHI-VersaProbe III system. Further,

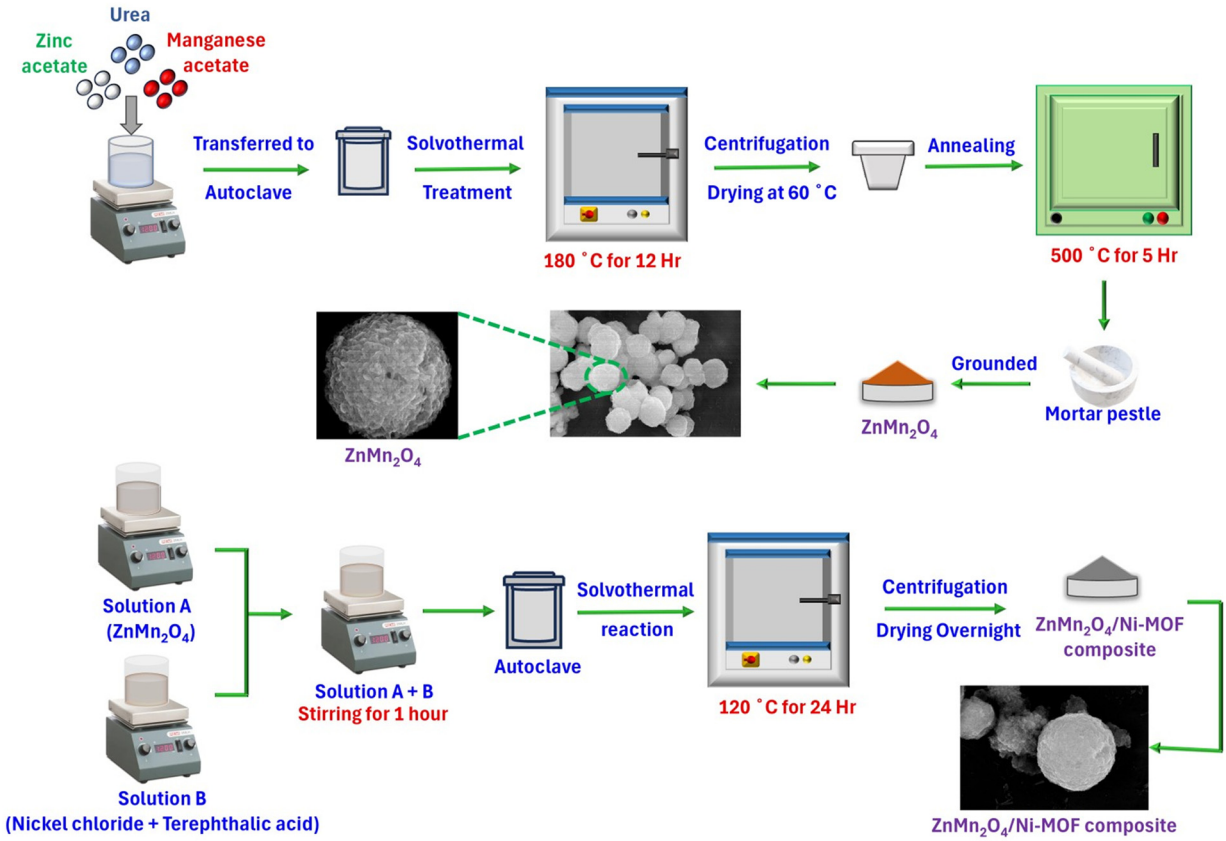

Fig. 1 Synthesis procedure of the $ZnMn_2O_4$/Ni-MOF composite.

the electrochemical properties of the $ZnMn_2O_4$/Ni-MOF composite were analysed *via* cyclic voltammetry (CV), galvanostatic charge–discharge (GCD), and electrochemical impedance spectroscopy (EIS), and they were assessed using an OrigaFlex OGF05A electrochemical workstation.

Preparation of electrodes for electrochemical measurements

The working electrode was prepared with a ratio of 8 : 1 : 1 of the active material, PVDF, and carbon black (serving as a binding agent and conductive additive). These components were meticulously combined with an NMP solvent and finely ground using an agate mortar to achieve a slurry-like consistency. The slurry was applied to the acid-cleaned nickel foam (NF) with a basic brushing method across a 1 × 1 cm area and allowed to dry overnight at 80 °C. The mass of the coated active material in NF was determined by subtracting the pre-coating mass of NF from the post-drying mass of the active material in the NF. The mass loading of the $ZnMn_2O_4$/Ni-MOF composite active material on the Ni foam substrate was ~2 mg. Mass loading was standardized across all electrodes to guarantee a dependable electrochemical comparison. The produced electrodes were subsequently employed for an electrochemical study to assess supercapacitance performance, using a platinum wire as the counter electrode, Ag/AgCl as the reference electrode, and 2 M KOH as the electrolyte.

Results and discussion

XRD patterns of the prepared $ZnMn_2O_4$, Ni-MOF, and the $ZnMn_2O_4$/Ni-MOF composite is shown in Fig. 2a. Spinel $ZnMn_2O_4$ shows diffraction peaks at 2θ values of 18.1°, 29.2°, 31.1°, 32.8°, 36.3°, 38.8°, 44.6°, 51.8°, 59.0°, 60.7°, and 65.1°, corresponding to the *hkl* values of (101), (112), (200), (103), (211), (004), (220), (105), (321), (224) and (400), respectively. These peaks match well with the tetragonal $ZnMn_2O_4$ with the $I4_1/amd$ space group (JCPDS No. 01-071-2499). The XRD pattern of Ni-MOF has peaks at 8.3°, 14.8°, 15.6°, and 16.8°, corresponding to the (200), (001), (201), and (−201) planes, respectively, which are in good agreement with prior literature results.[17] The XRD pattern of the $ZnMn_2O_4$/Ni-MOF composite confirms the presence of both $ZnMn_2O_4$ and Ni-MOF without any impurities. The average crystalline size (D) is calculated using the Scherrer formula:

$$D = \frac{0.9\lambda}{\beta \cos \theta}. \quad (1)$$

The average crystallite size of the prepared $ZnMn_2O_4$, Ni-MOF, and $ZnMn_2O_4$/Ni-MOF is found to be 14.2 nm, 8.1 nm, and 10.8 nm, respectively.

The FTIR spectrum of $ZnMn_2O_4$ (Fig. 2b) exhibit characteristic peaks at 406, 505, and 621 cm^{-1}, corresponding to meta-oxygen vibrations. The band around 621 cm^{-1} is attributed to

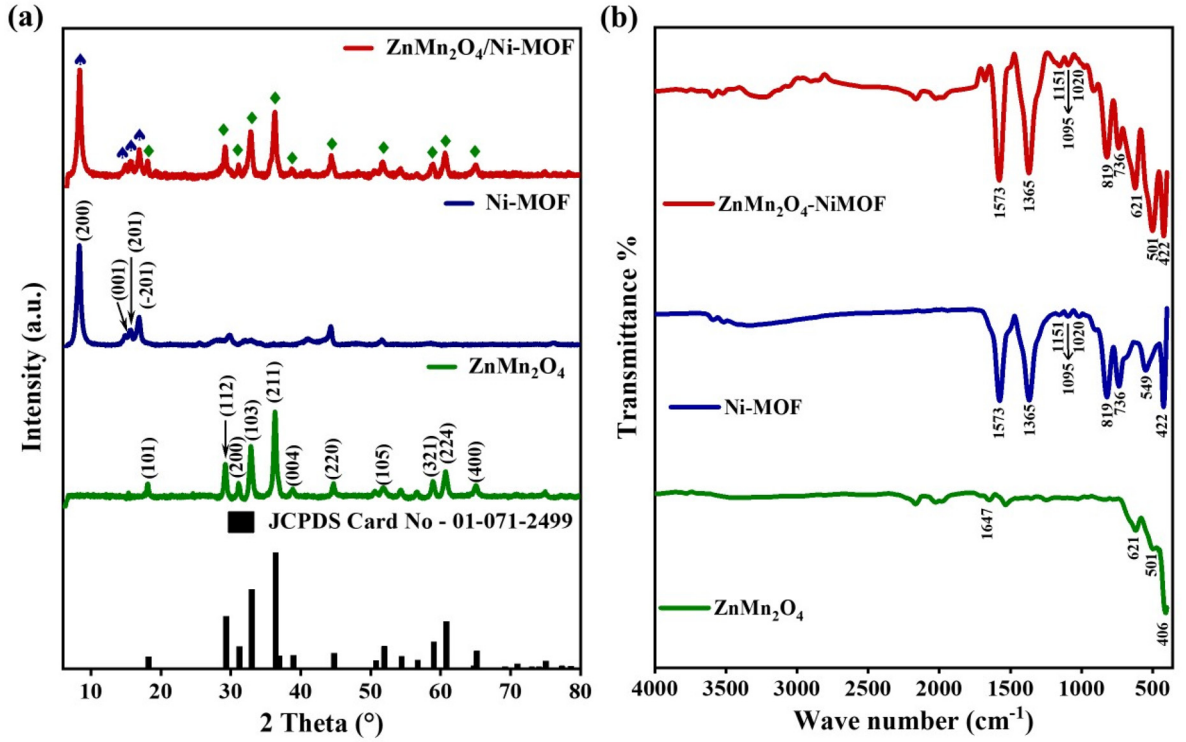

Fig. 2 (a) X-ray diffractograms of $ZnMn_2O_4$, Ni-MOF, and the $ZnMn_2O_4$/Ni-MOF composite, and (b) FTIR spectra of $ZnMn_2O_4$, Ni-MOF, and the $ZnMn_2O_4$/Ni-MOF composite.

tetrahedral Zn-O stretching, while the peaks near 505 and 406 cm^{-1} are associated with octahedral Mn–O vibrations and lattice M–O–M bonding.[18] A weak band at 1647 cm^{-1} is due to the C=C stretching vibration.[19] The Ni-MOF spectrum exhibits an absorption at 442 cm^{-1}, which is ascribed to metal–oxygen–hydrogen bending vibrations.[20] A weak band at 549 cm^{-1} is assigned to Ni–O stretching vibrations, confirming metal–oxygen coordination in the MOF framework.[21] The characteristic benzene ring's *para*-position vibrations at 736 and 819 cm^{-1} are related to bending vibrations of aromatic C–H groups, along with peaks at 1020, 1095, and 1151 cm^{-1} assigned to C–O stretching of carboxylate groups.[22] The peaks at 1365 and 1573 cm^{-1} correspond to the symmetric and asymmetric stretching modes of coordinated carboxylates. This signifies that the $-COO^-$ of H_2BDC is coordinated to Ni^{2+} *via* a bidentate ligand mode.[23] The FTIR spectra of the composite ($ZnMn_2O_4$/Ni-MOF) display peaks that belong to both $ZnMn_2O_4$ and Ni-MOF. These findings indicate that the two components are fully integrated and have formed a composite structure.

HR-SEM is used to comprehensively analyse the morphology and microstructure of the $ZnMn_2O_4$/Ni-MOF composite material (Fig. 3a–c), which exhibits a consistent size distribution and morphology. The HR-SEM images reveal a combination of dominant spherical microstructures of $ZnMn_2O_4$ and hierarchical flake-like sponges of Ni-MOF in the composite. The morphological characteristics of $ZnMn_2O_4$/Ni-MOF at higher magnification is emphasised, revealing a significant structural alteration with linked Ni-MOF nano-sponges enveloping the $ZnMn_2O_4$ microspheres. The unique morphology is expected to enhance the surface area, promote electrochemical performance, and provide space to accommodate strains during charge–discharge processes, thus improving the stability.[24] Further, the elemental mapping (Fig. 3d–i) confirms the existence and distribution of Zn, Mn, Ni, C, and O elements. Energy dispersive X-ray spectroscopy (EDX) analysis (Fig. 3j) displays the elemental percentages of the composite, confirming the absence of impurities. Morphological analysis of the pure $ZnMn_2O_4$ and Ni-MOF is also compared and shown in the Fig. S1 and S2.

The XPS analysis of the $ZnMn_2O_4$/Ni-MOF composite confirmed the existence of Zn, Mn, Ni, C, and O elements, as shown in Fig. 4a, providing significant knowledge into their oxidation states. The high-resolution Zn 2p spectra (Fig. 4b) exhibit two characteristic peaks at 1021.3 eV (Zn $2p_{3/2}$) and 1044.45 eV (Zn $2p_{1/2}$), with a spin–orbital splitting of ~23.1 eV, which confirms Zn^{2+} oxidation state. The Zn^{2+} ion plays a structurally stabilizing role within the spinel lattice rather than contributing directly to faradaic charge storage.[25] The Mn 2p spectrum exhibits doublets with binding energies of 641.7 eV and 652.9 eV for the Mn $2p_{3/2}$ and Mn $2p_{1/2}$ levels, respectively, suggesting a binding energy difference of ~11.2 eV, which corresponds to the Mn^{2+} oxidation state. The two satellite peaks at 644.2 (Mn $2p_{3/2}$) and 654.2 eV (Mn $2p_{1/2}$) are attributed to the Mn^{3+} oxidation state, as shown in Fig. 4c. The coexistence of Mn^{2+} and Mn^{3+} indicates mixed-valence manganese

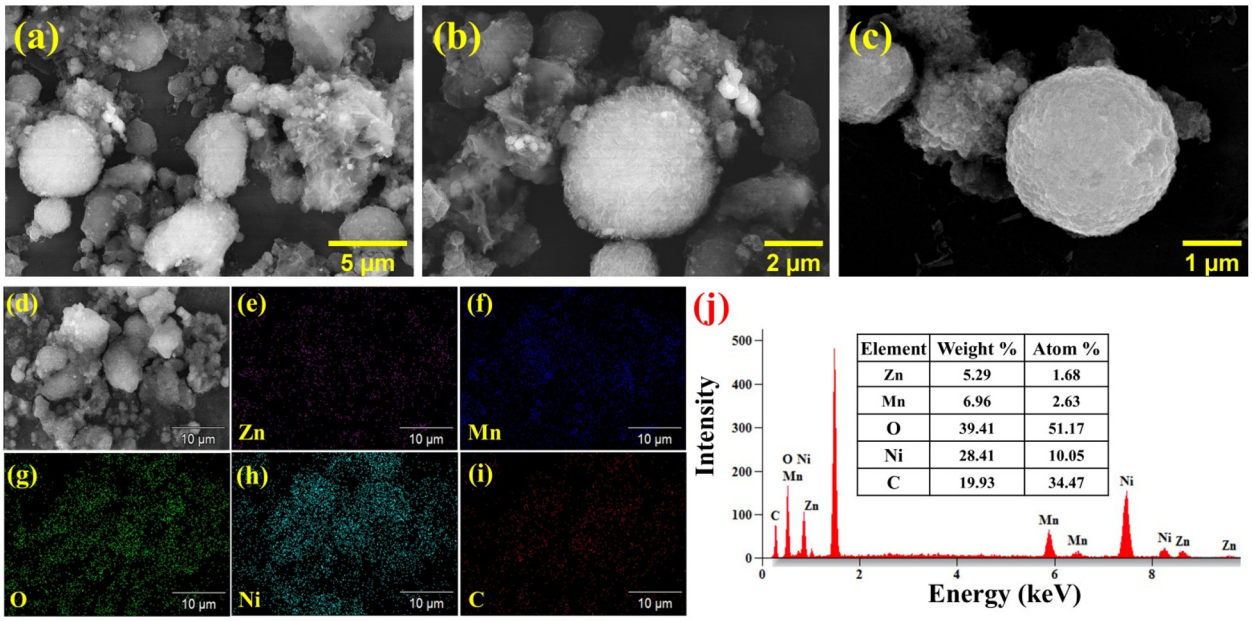

Fig. 3 (a–c) HR-SEM images of the $ZnMn_2O_4$/Ni-MOF nanocomposite at different magnifications, (d–i) elemental mapping images, and (j) EDX spectrum and elemental composition of the $ZnMn_2O_4$/Ni-MOF nanocomposite.

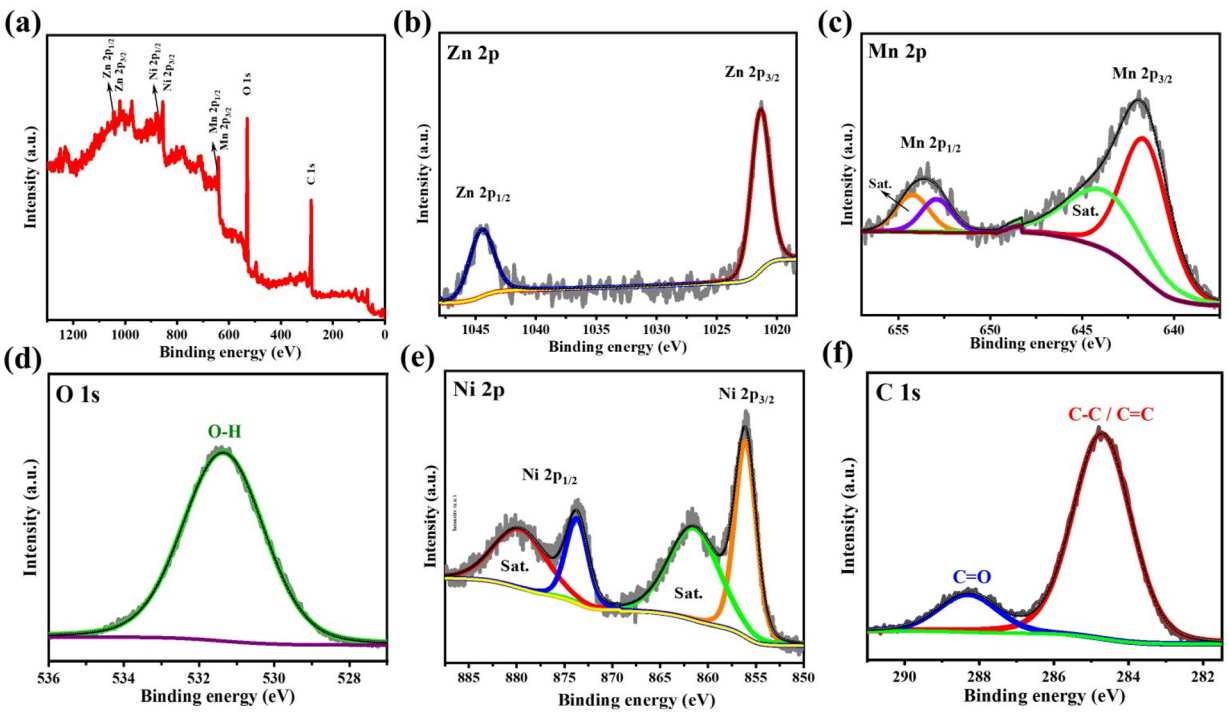

Fig. 4 (a) XPS survey spectrum of the $ZnMn_2O_4$/Ni-MOF composite, and (b–f) XPS spectra of Zn 2p, Mn 2p, O 1s, Ni 2p, and C 1s.

within the $ZnMn_2O_4$ phase, which is highly advantageous for pseudocapacitive energy storage as it enables multiple reversible redox reactions during charge–discharge processes.[14,26] The O 1s spectra (Fig. 4d) show a dominant peak centred at 531.3 eV, corresponding to the hydroxyl (OH) bond and defect-related oxygen species. Such oxygen-containing functional groups are known to enhance electrolyte wettability and facilitate ion diffusion.[27] The Ni 2p spectra (Fig. 4e) show two distinct peaks at 856.1 eV and 873.7 eV, representing the Ni $2p_{3/2}$ and Ni $2p_{1/2}$ states, respectively, with an energy separation of ~17.6 eV, and two satellite peaks are seen at 861.6 eV and 879.9 eV, corresponding to the Ni^{3+} and Ni^{2+} oxidation states,

confirming the redox active nature of Ni-MOF. The reversible Ni^{2+}/Ni^{3+} redox couple contributed significantly to the faradaic capacitance of the composite.[28] In C 1s spectra, the peaks at 288.2 and 284.7 eV are due to the aromatic ring and carboxylic acid group of the terephthalic acid ligand and are associated with C–C and C═O, respectively (Fig. 4f).[29] The coexistence of multiple oxidation states in both Mn and Ni, as revealed by XPS, provides abundant redox-active sites and underpins the synergistic charge-storage behavior observed in the $ZnMn_2O_4$/Ni-MOF composite electrode.

In electrochemical studies, the CV curves of the $ZnMn_2O_4$/Ni-MOF composite were recorded at different scan rates from 10 to 50 mV s^{-1} within a potential range of 0.8 V (*vs.* Ag/AgCl) in 2 M KOH, as shown in Fig. 5a. The CV curves at increasing scan rates show discrete redox peaks, confirming the typical pseudocapacitive behaviour characterised by rapid charge-transfer kinetics. The redox peaks are mostly attributed to faradaic oxidation and reduction reactions between the composite and hydroxyl ions. These reactions illustrate that electrolyte cations (K^+) can adsorb onto the surface or be intercalated/deintercalated within the voids of the spinel structure at the oxide-electrolyte interface. Redox processes occur when K^+ ions are added to the electrode material from the electrolyte during charging and released back into the electrolyte during discharging.[18] The redox activity of manganese ions predominantly dictates the electrochemical properties of $ZnMn_2O_4$ in the alkaline electrolyte, whereas zinc remains electrochemically inactive. During CV, the Mn centres participate in reversible oxidation and reduction processes with hydroxide ions, as shown in eqn (2)–(4).[15]

$$(ZnMn_2O_4)_{Surface} + K^+ + e^- \rightarrow [KZnMn_2O_4]_{Surface} \quad (2)$$

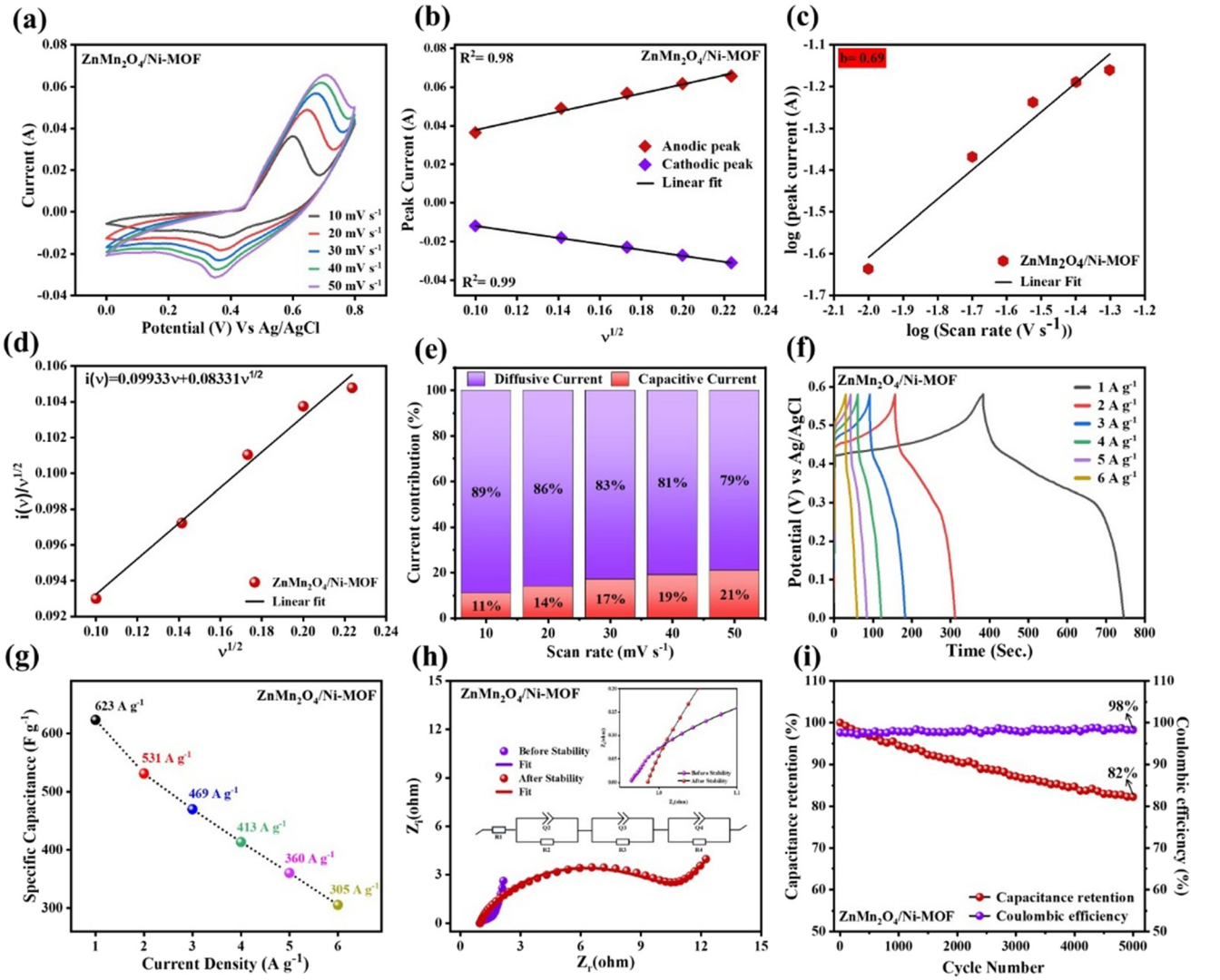

Fig. 5 (a) CV at different scan rates, (b) relation between i_p and the square root of scan rate, (c) *b*-value (slope) calculated from the plot between log (i_p) *versus* log(ν), (d) k_1 (slope) and k_2 (intercept) values calculated using the Dunn's equation, (e) current contribution bar graph, (f) GCD curves at different current densities, (g) specific capacitance (C_s) for various current densities, (h) impedance spectra (inset: R_s region of EIS spectra), and (i) cycling stability of the $ZnMn_2O_4$/Ni-MOF composite after 5000 cycles.

$$ZnMn_2O_4 + K^+ + e^- \rightarrow [ZnMn_2O_4]K \quad (3)$$

$$2MnOOH + 2OH^- \leftrightarrow 2MnO_2 + 2H_2O + 2e^- \quad (4)$$

In Ni-MOF, the redox peaks are derived from the faradaic reaction between Ni^{2+} and Ni^{3+} as shown in eqn (5) and (6).[30] The faradaic redox processes of OH^- intercalation and de-intercalation at the surface are responsible for the pseudocapacitive properties.[21]

$$Ni(OH)_2 + OH^- \rightarrow NiOOH + H_2O + e^- \quad (5)$$

$$NiOOH + OH^- \rightarrow NiO_2 + H_2O + e^- \quad (6)$$

Consequently, the composite demonstrates enhanced redox activity owing to the synergistic effects of both transition-metal centres, resulting in an improved pseudocapacitive response.

The Randles–Sevcik equation is employed for determining the relationship between the peak current (i_p) and the square root of the scan rate ($\nu^{1/2}$) for both anodic and cathodic responses. Notably, as the scan rate escalates, the anodic and cathodic peaks progressively move towards higher positive and negative potentials due to the polarization effect within the electrode, while the reduction and oxidation peaks move towards lower and higher potentials, respectively. This shows that the electrochemical process is highly reversible and has greater potential separation, even though the shape of the CV curves remains the same.[31] As the scan rate increases from 10 to 50 mV s^{-1}, the anodic peak of the $ZnMn_2O_4$/Ni-MOF composite moves from 0.59 V to 0.70 V, with a possible shift of 0.11 V, as shown in Fig. 5b. The observed positive shift in anodic peak potentials for the $ZnMn_2O_4$/Ni-MOF composite indicates its unique pseudocapacitive behaviour influenced by electrochemical kinetics.[32]

To provide additional insights into the charge-storage mechanism, the *b*-value is calculated using the equation $i_p = a\nu^b$. The *b*-value of the $ZnMn_2O_4$/Ni-MOF composite is found to be 0.69 by plotting $\log(i_p)$ against $\log(\nu)$, showing a mixed charge-storage mechanism with a dominant pseudocapacitive behaviour rather than pure battery-type behavior, indicating a surface- and diffusion-controlled faradaic mechanism, as illustrated in the Fig. 5c.[33] Dunn's approach is utilised to quantify the current contributions from both surface-controlled and diffusion-controlled processes using eqn (S1) and (S2) in the composite (Fig. 5d). The investigation indicated that, even at a reduced scan rate of 10 mV s^{-1}, diffusive-controlled charge storage predominates in $ZnMn_2O_4$/Ni-MOF electrodes, with a diffusive current contribution of 89% (11% for capacitive current). The bar graph indicates that, as the scan rate increases from 10 to 50 mV s^{-1}, the diffusion-controlled current reduces from 89% to 79% due to increased internal diffusion resistance, as shown in Fig. 5e. When the scan rate reaches 50 mV s^{-1}, the $ZnMn_2O_4$/Ni-MOF composite shows 79% to diffusion and 21% to capacitive contribution. This behaviour aligns with the significant pseudocapacitive contribution, which is crucial to their electrochemical performance.[34] The CV plots at 10 and 50 mV s^{-1}, which explain the current contribution of $ZnMn_2O_4$/Ni-MOF, are shown in Fig. S3a and b.

Galvanostatic charge–discharge (GCD) measurements are conducted for the $ZnMn_2O_4$/Ni-MOF composite with a potential of 0.58 V (*vs.* Ag/AgCl) at current densities from 1 to 6 A g^{-1}, as illustrated in Fig. 5f. The resultant potential-time profiles exhibit remarkable balance across all current densities, reflecting highly reversible redox processes, minimum polarisation, and excellent coulombic efficiency. These results are consistent with the CV studies, demonstrating strong pseudocapacitive behaviour. Fig. 5g illustrates the specific capacitance values of the $ZnMn_2O_4$/Ni-MOF composite derived from the GCD curves. The $ZnMn_2O_4$/Ni-MOF composite exhibits specific capacitance values of 623, 531, 469, 413, 360, and 305 F g^{-1} for current densities ranging from 1 to 6 A g^{-1}, calculated using eqn (S3). These values are higher compared to those reported in previous studies, as shown in Table S1. These findings highlight the exceptional electrochemical performance of the $ZnMn_2O_4$/Ni-MOF composite, attributed to the synergistic interaction between Zn, Ni, and Mn atoms, which exhibit multiple valence states and promote faradaic reactions.

Electrochemical impedance spectroscopy (EIS) is performed over a frequency range of 100 kHz to 100 mHz to investigate the electrode material's electron-transfer kinetics, interfacial interactions, and capacitive properties, with the resulting Nyquist plot shown in Fig. 5h. Examination of the Nyquist plot using the analogous circuit (inset of Fig. 5h) provided significant insights into the material's resistive and capacitive characteristics. The solution resistance (R_s) of the composite in the NF is determined by identifying the intercept on the real axis in the high-frequency region and is recorded at 0.96 Ω before cycling, marginally increasing to 0.98 Ω post-cycling. The semicircular diameter on the curve represents the charge-transfer resistance (R_{ct}), while the diameter signifies the material's conductivity. The R_{ct} at the interface between the electrode surface and the electrolyte is measured at 1.62 Ω before cycling and 10.7 Ω after cycling. This significant increase in R_{ct} indicates cycling-induced degradation at the electrode–electrolyte interface, potentially caused by partial surface passivation, a reduction in electrochemically active sites, or structural deterioration of the electrode during repeated charge–discharge cycles, resulting in impeded interfacial charge transfer. The capacitance retention (CR) and coulombic efficiency (CE) of the $ZnMn_2O_4$/Ni-MOF composite electrode material are assessed through 5000 charge–discharge cycles. Upon cycling at a current density of 10 A g^{-1}, the electrode demonstrated a retention of 82% and a coulombic efficiency of 98% using eqn (S4), indicating its improved stability as shown in Fig. 5i. To provide further insight, the electrochemical studies of pure $ZnMn_2O_4$ and Ni-MOF were taken and shown in Fig. S4 & S5.

Post-cycling structural studies are carried out to understand the structural and morphological stability of the $ZnMn_2O_4$/Ni-MOF electrode. Fig. S6 displays the XRD patterns, with the detected peaks corresponding to $ZnMn_2O_4$/Ni-MOF and NF on which the active material is deposited. The intense peaks are

accompanied by sharp peaks arising from the nickel foam. The diffraction peaks correspond to (220), (−201), (103), and (211) planes of $ZnMn_2O_4$/Ni-MOF, confirming the structural stability of the composite with no phase change even after 5000 cycles. However, there is a gradual reduction in the crystallinity of the composite due to prolonged cyclic stability. Moreover, the development of the NF's hydroxide layer reduces the responses from the active material. However, the presence of characteristics peaks signifies that the active material does not entirely decompose and retains its structural integrity despite reduced crystallinity. Moreover, *ex situ* HR-SEM images (Fig. S7) reveal negligible alteration to the material's morphology after stability. EDS analysis reveals the presence of Zn, Mn, Ni, O, C, and trace amounts of K resulting from K^+ ions in 2 M KOH. The combined results demonstrate the remarkable structural and morphological stability of the $ZnMn_2O_4$/Ni-MOF electrode, rendering it a highly reliable and superior material for electrochemical applications.

Owing to the superior performance of the $ZnMn_2O_4$/Ni-MOF composite in a three-electrode configuration, we developed an aqueous asymmetric supercapacitor (AASC) utilising a two-electrode system, with activated carbon (AC) serving as the anode and the $ZnMn_2O_4$/Ni-MOF composite as the cathode. The electrochemical analyses of the AC are conducted by utilising a three-electrode setup, as depicted in Fig. S8. The working voltage of 1.6 V is determined by comparing the CV curves of AC and the $ZnMn_2O_4$/Ni-MOF composite, as shown in the three-electrode system, which exhibits a combination of electric double-layer capacitance (EDLC) and pseudocapacitance. At lower scan rates, prominent redox peaks are seen; however, with an increase in the scan rate, the redox peaks were less prominent, as shown in the Fig. 6a. GCD analyses for the AASC were conducted at different current densities of 1 to 2.5 A g^{-1} (Fig. 6b), delivering a C_s of 155 to 99 F g^{-1}, as shown in the Fig. 6c. It achieved a maximum energy density of 55 Wh kg^{-1} and power density of 800 W kg^{-1} (Fig. 6d), calculated using eqn (S6) and (S7). The Nyquist plots of the AASC (Fig. 6e) display a distinct semicircle in the high-frequency domain, indicating the existence of both solution resistance (R_s) and charge-transfer resistance (R_{ct}). The R_s levels recorded before and after the stability test were found to be 3.98 Ω and 11 Ω, respectively, while the associated R_{ct} values increased from 4.85 Ω to 30.11 Ω. Increased resistance upon cycling can be ascribed to slight structural or interfacial alterations within the electrode–electrolyte system. Furthermore, the AASC exhibited remarkable electrochemical stability of 80% and achieved a high coulombic efficiency of 96% after 5000 cycles at a current density of 5 A g^{-1}, as shown in Fig. 6f. These findings validate the enhanced stability, effective ion transport, and consistent performance of the AASC device at higher current conditions.

An asymmetric supercapacitor (ASC) device is constructed utilising activated carbon as the negative electrode and the $ZnMn_2O_4$/Ni-MOF composite as the positive electrode, with a Whatman filter paper separator dipped in a PVA/KOH gel electrolyte. The CV profiles (Fig. 7a) demonstrated a combination of EDLC and pseudocapacitive behaviour, with pseudo-

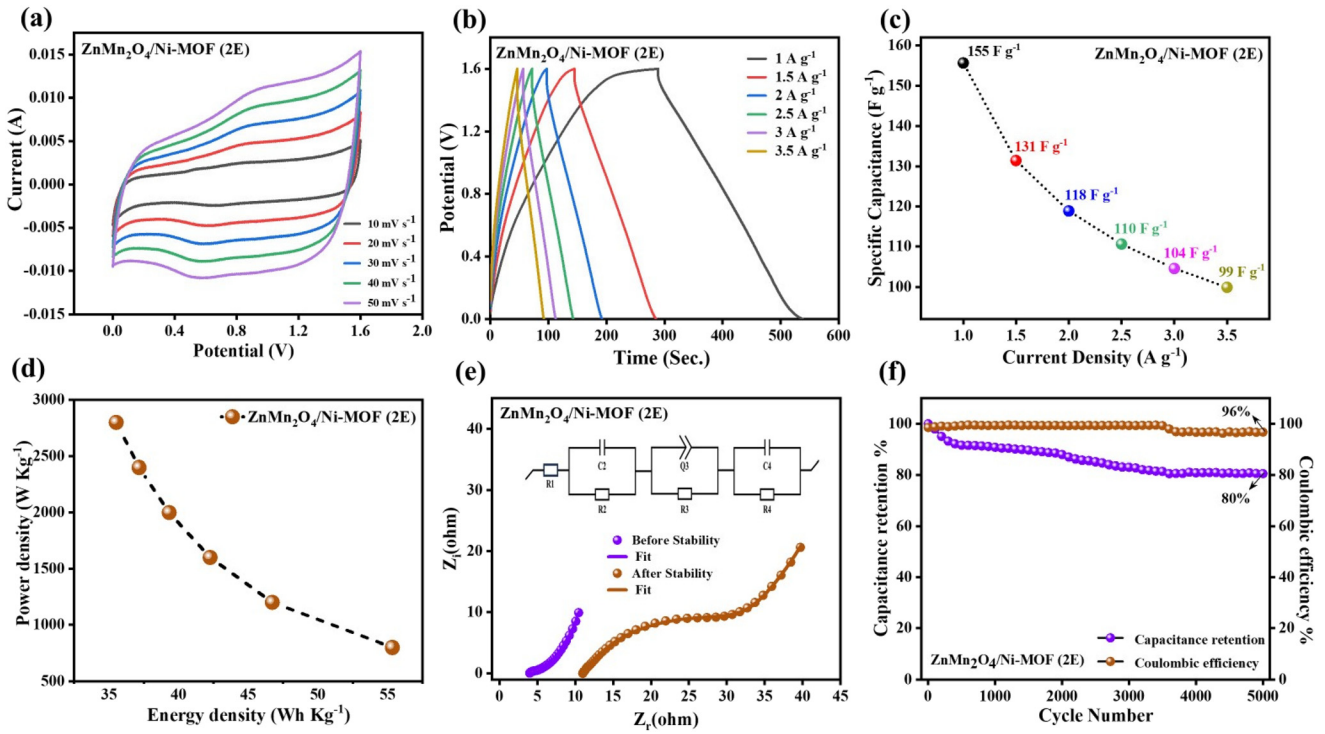

Fig. 6 Two electrode configurations of the $ZnMn_2O_4$/Ni-MOF composite: (a) CV curves, (b) GCD curves, (c) specific capacitance (C_s) at various current densities, (d) Ragone plot of the AASC, (e) impedance spectra before and after 5000 cycles, and (f) cycling stability tested over 5000 cycles at 5 Ag^{-1}.

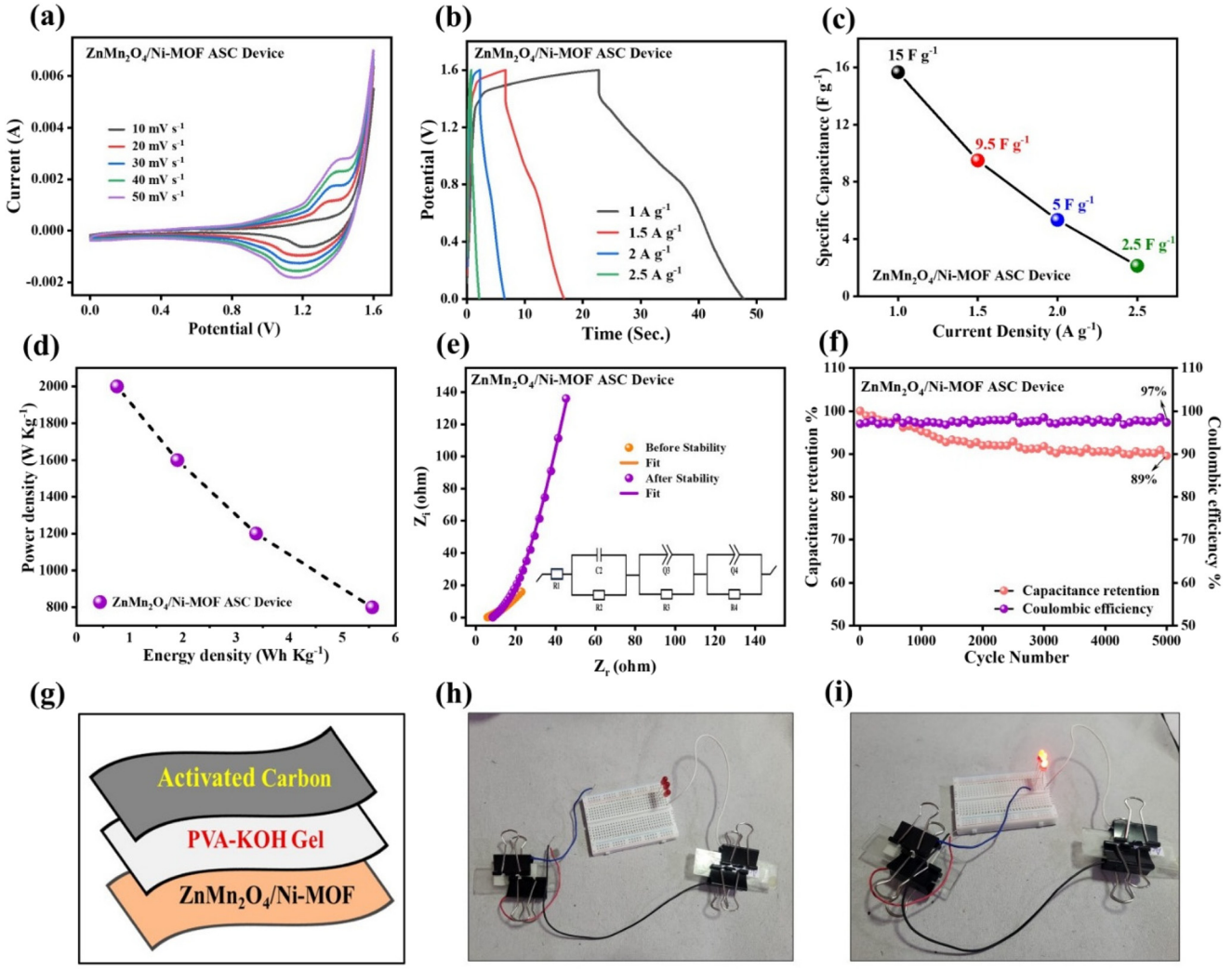

Fig. 7 Fabricated $ZnMn_2O_4$/Ni-MOFASC device: (a) CV curves, (b) GCD curves, (c) specific capacitance (C_s) at various current densities, (d) Ragone plot, (e) EIS before and after 5000 cycles, (f) cyclic stability over 5000 cycles, (g) ASC device, (h–i) LEDs powered using the fabricated ASC devices.

capacitive being the dominant contribution. As scan rates increased from 10 to 50 mV s^{-1}, the intensity of the redox peaks progressively diminished, signifying a transition towards capacitive charge storage. The GCD curves at different current densities (Fig. 7b) exhibited symmetric profiles, indicating excellent reversibility. The ASC attained a peak C_s of 15 F g^{-1} at 1 A g^{-1} (Fig. 7c) and demonstrated an energy density of 5.5 Wh kg^{-1} alongside a power density of 800 W kg^{-1} (Fig. 7d). The Nyquist plot of the constructed ASC device (Fig. 7e) shows that the R_s values increased from 5.9 Ω before cycling to 13 Ω post cycling, while the R_{ct} values rose from 8.49 Ω to 31.9 Ω. The nearly vertical line in the low-frequency range and the smaller imaginary component indicate that ions are diffusing rapidly and that there is low resistance to diffusion at the electrode–electrolyte interface. These EIS results show that the constructed ASC has high electrical contact, low ionic resistance, and steady charge-transfer properties, all of which help it function better electrochemically.[35] Following 5000 charge–discharge cycles at 4 A g^{-1}, the device maintained 97% of its capacitance with a coulombic efficiency of 89% (Fig. 7f), indicating remarkable stability and potential for portable energy storage applications. The practical applicability of the developed ASC (Fig. 7h) is demonstrated by its ability to energise several red LEDs using two ASCs, as illustrated in Fig. 7i–j and S9. These experiments highlight the potential of the prepared composite electrode materials for practical applications.

Conclusions

This study conclusively shows that the solvothermal synthesis of the $ZnMn_2O_4$/Ni-MOF composite yields a high-performance electrode material with remarkable electrochemical characteristics. In a three-electrode system, the composite demonstrated an exceptional C_s value of 623 F g^{-1} at 1 A g^{-1}, with cycling stability of 82% capacitance retention and a coulombic

efficiency of 98% after 5000 cycles. The electrode's structural and morphological stability is examined through post-cycling XRD and SEM analyses. The AASC shows a C_s of 155 F g^{-1} at 1 A g^{-1} and provides notable energy and power densities in an asymmetric arrangement. An asymmetric supercapacitor (ASC) device is constructed and shows a C_s of 15 F g^{-1} at 1 A g^{-1}. The effective functioning of the built ASC devices in powering LEDs underscores the practical usefulness of this material for real-world energy storage applications. The $ZnMn_2O_4$/Ni-MOF composite emerges as a superior alternative for next-generation electrochemical energy storage devices, effectively reconciling high performance with practical usability.

Author contributions

A. K: writing – original draft, conceptualization, visualization, methodology, validation, investigation, formal analysis, data curation. K. B. K.: writing – review & editing. G. A.: supervision, validation, and writing – review & editing.

Conflicts of interest

The authors declare no conflicts of interest.

Data availability

The data supporting this article have been included as part of the supplementary information (SI). Supplementary information is available. See DOI: https://doi.org/10.1039/d5nr04623h.

Acknowledgements

We thank the SRM Institute of Science and Technology, Kattankulathur-603203, and the Directorate of Research, SRMIST, for their financial support in the form of a Doctoral Research Fellowship, and the Department of Physics and Nanotechnology for providing the required infrastructure and electrochemical instruments. The authors also acknowledge the PNCF (Physics and Nanotechnology Characterization Facility), SCIF (SRM Central Instrumentation Facility), and NRC (Nanotechnology Research Centre), SRMIST, for providing the instrumentation facilities.

References

1 P. Rosaiah, N. Maaouni, M. Goddati, J. Lee, S. Sambasivam, M. R. Karim, I. A. Alnaser, V. R. M. Reddy and W. K. Kim, *J. Energy Storage*, 2024, **76**, 109636.
2 M. R. Pallavolu, C. V. V. Muralee Gopi, S. Prabu, P. R. Ullapu, J. H. Jung, S. W. Joo and R. Ramesh, *RSC Adv.*, 2025, **15**, 4619–4627.
3 X. Zhao, L. Mao, Q. Cheng, J. Li, F. Liao, G. Yang, L. Xie, C. Zhao and L. Chen, *Chem. Eng. J.*, 2020, **387**, 124081.
4 J. Palraj and H. A. Therese, *J. Energy Storage*, 2025, **107**, 114957.
5 T. B. Naveen, D. Durgalakshmi, S. Balakumar and R. A. Rakkesh, *Chem. Commun.*, 2024, **60**, 208–211.
6 T. Ramachandran, S. S. Sana, K. D. Kumar, Y. A. Kumar, H. H. Hegazy and S. C. Kim, *J. Energy Storage*, 2023, **73**, 109096.
7 Y. Xiao, W. Wei, M. Zhang, S. Jiao, Y. Shi and S. Ding, *ACS Appl. Energy Mater.*, 2019, **2**, 2169–2177.
8 G. B. Bhanuse, S. Kumar, C.-W. Chien and Y.-P. Fu, *Electrochim. Acta*, 2025, **511**, 145371.
9 J. Yang, C. Zheng, P. Xiong, Y. Li and M. Wei, *J. Mater. Chem. A*, 2014, **2**, 19005–19010.
10 A. Kumararaj, M. J. Kennedy, L. Baskar, G. Arunachalam, R. Pachaiappan, S. K. Saxena, R. Rajendran and K. Manavalan, *Electric and Electronic Applications of Metal Oxides*, Elsevier, 2025, pp. 127–169.
11 P. E. Saranya and S. Selladurai, *J. Mater. Sci.: Mater. Electron.*, 2018, **29**, 3326–3339.
12 M. P. Mani, V. Venkatachalam, K. Thamizharasan and M. Jothibas, *J. Electron. Mater.*, 2021, **50**, 4381–4387.
13 C. Zhang, D. Chen, Y. Luo, Y. Yuan, Y. Wang and Z. Yang, *Surf. Interfaces*, 2025, **56**, 105517.
14 P. Deva, S. Ravi and C. Manoharan, *Emergent Mater.*, 2024, **7**, 2407–2421.
15 V. Sannasi and K. Subbian, *Ceram. Int.*, 2021, **47**, 12300–12309.
16 A. S. Eliwa, S. S. Medany, G. G. Mohamed and M. A. Hefnawy, *J. Inorg. Organomet. Polym. Mater.*, 2025, **35**, 4797–4809.
17 A. Cao, L. Zhang, Y. Wang, H. Zhao, H. Deng, X. Liu, Z. Lin, X. Su and F. Yue, *ACS Sustainable Chem. Eng.*, 2019, **7**, 2492–2499.
18 D. Patel, S. N. Bariya, Y. G. Kapdi, P. Patel, A. Patel, V. Solanki, S. S. Soni and M. H. Patel, *J. Alloys Compd.*, 2025, **1014**, 178519.
19 N. Senthilkumar, V. Venkatachalam, M. Kandiban, P. Vigneshwaran, R. Jayavel and I. Vetha Potheher, *Physica E Low. Dimens. Syst. Nanostruct.*, 2019, **106**, 121–126.
20 M. G. Radhika, B. Gopalakrishna, K. Chaitra, L. K. G. Bhatta, K. Venkatesh, M. K. Sudha Kamath and N. Kathyayini, *Mater. Res. Express*, 2020, **7**, 054003.
21 P. G. Raje, S. R. Gurav, M. R. Waikar, G. R. Chodankar, U. V. Shembade, A. V. Moholkar, T. D. Dongale and R. G. Sonkawade, *J. Energy Storage*, 2024, **95**, 112617.
22 G. B. Bhanuse, S. Kumar, C.-W. Chien and Y.-P. Fu, *Electrochim. Acta*, 2025, **511**, 145371.
23 Y. Xiao, W. Wei, M. Zhang, S. Jiao, Y. Shi and S. Ding, *ACS Appl. Energy Mater.*, 2019, **2**, 2169–2177.
24 G. B. Bhanuse, S. Kumar, C.-W. Chien and Y.-P. Fu, *Electrochim. Acta*, 2025, **511**, 145371.
25 F. Gao, B. Mei, X. Xu, J. Ren, D. Zhao, Z. Zhang, Z. Wang, Y. Wu, X. Liu and Y. Zhang, *Chem. Eng. J.*, 2022, **448**, 137742.

26 A. Samage, P. Kuppe, M. Halakarni, B. K. Ganesan, S. V. Kamath, H. Yoon and N. S. Kotrappanavar, *J. Energy Storage*, 2024, **97**, 112934.
27 P. Rosaiah, N. Maaouni, M. Goddati, J. Lee, S. Sambasivam, M. R. Karim, I. A. Alnaser, V. R. M. Reddy and W. K. Kim, *J. Energy Storage*, 2024, **76**, 109636.
28 M. A. Yewale, R. A. Kadam, N. K. Kaushik, S. V. P. Vattikuti, L. P. Lingamdinne, J. R. Koduru and D. K. Shin, *Ceram. Int.*, 2022, **48**, 21996–22005.
29 J. Lu, Q. Liu, K. Xu, R. Zou and C. Wang, *Russ. J. Phys. Chem. A*, 2024, **98**, 323–330.
30 X. Xiong, D. Ding, D. Chen, G. Waller, Y. Bu, Z. Wang and M. Liu, *Nano Energy*, 2015, **11**, 154–161.
31 W. Liu, X. Li, M. Zhu and X. He, *J. Power Sources*, 2015, **282**, 179–186.
32 A. Kumararaj, S. Perumal, K. B. Karuppanan and G. Arunachalam, *ChemNanoMat*, DOI: 10.1002/cnma.202500207.
33 K. Li, H. Teng, Q. Sun, Y. Li, X. Wu, X. Dai, Y. Wang, S. Wang, Y. Zhang, K. Yao, Z. Bao, J. Rao and Y. Zhang, *J. Energy Storage*, 2022, **53**, 105094.
34 N. T. Bharanitharan, D. Dhinasekaran, M. R. A. Kishore, B. Subramanian and A. R. Rajendran, *Chem. Eng. J.*, 2025, **518**, 164556.
35 K. Subramani, N. Sudhan, R. Divya and M. Sathish, *RSC Adv.*, 2017, **7**, 6648–6659.